Ad Hoc Networks xxx (2008) xxx–xxx

Contents lists available at ScienceDirect

Ad Hoc Networks

journal homepage: www.elsevier.com/locate/adhoc

Three-dimensional and two-dimensional deployment analysis for underwater acoustic sensor networks ☆

Dario Pompili [a,*], Tommaso Melodia [b], Ian F. Akyildiz [c]

[a] Department of Electrical and Computer Engineering Rutgers, The State University of New Jersey, 94, Brett Road, Piscataway, NJ 08854, United States
[b] Department of Electrical Engineering University at Buffalo, The State University of New York, 332, Bonner Hall, Buffalo, NY 14260, United States
[c] Broadband Wireless Networking Laboratory, School of Electrical and Computer Engineering, Georgia Institute of Technology, 75, 5th Street, Atlanta, GA 30332, United States

ARTICLE INFO

Article history:
Received 8 October 2007
Received in revised form 11 February 2008
Accepted 23 July 2008
Available online xxxx

Keywords:
Underwater acoustic sensor networks
Deployment
Sensing coverage

ABSTRACT

Underwater sensor networks find applications in oceanographic data collection, pollution monitoring, offshore exploration, disaster prevention, assisted navigation, and tactical surveillance. In this paper, deployment strategies for two-dimensional and three-dimensional communication architectures for underwater acoustic sensor networks are proposed, and a mathematical deployment analysis for both architectures is provided. The objective is to determine the minimum number of sensors to be deployed to achieve optimal sensing and communication coverage, which are dictated by application requirements; provide guidelines on how to choose the optimal deployment surface area, given a target body of water; study the robustness of the sensor network to node failures, and provide an estimate of the number of redundant sensor nodes to be deployed to compensate for potential failures.

1. Introduction

Underwater sensor networks are envisioned to enable applications for oceanographic data collection, ocean sampling, environmental and pollution monitoring, offshore exploration, disaster prevention, tsunami and seaquake warning, assisted navigation, distributed tactical surveillance, and mine reconnaissance. There is, in fact, significant interest in monitoring aquatic environments for scientific, environmental, commercial, safety, and military reasons. While there is a need for highly precise, real-time, fine grained spatio-temporal sampling of the ocean environment, current methods such as remote telemetry and sequential local sensing cannot satisfy many application needs, which call for wireless underwater acoustic networking. Underwater acoustic sensor networks (UW-ASN) [1] consist of sensors that are deployed to perform collaborative monitoring tasks over a given body of water. UW-ASN communication links are based on *acoustic wireless technology*, which poses unique challenges because of the harsh underwater environment such as limited bandwidth capacity [10], high and variable propagation delays [6], high bit error rates, and temporary losses of connectivity caused by multipath and fading phenomena [11].

In this paper, we consider two communication architectures for UW-ASNs, which were introduced in [1], i.e., the *two-dimensional architecture*, where sensors are anchored to the bottom of the ocean, and the *three-dimensional architecture*, where sensors float at different ocean depths covering the entire monitored volume region. While the former is designed for networks whose main objective is to monitor the ocean bottom, the latter is more suitable to detect and observe phenomena in the three-dimensional space that cannot be adequately observed by means

☆ A preliminary version of this paper was accepted for publication in Proceedings of the ACM International Workshop on UnderWater Networks (WUWNet), Los Angeles, CA, September 2006 [4].

* Corresponding author. Tel.: +1 732 445 6400x202; fax: +1 732 445 0593.
E-mail addresses: pompili@ece.rutgers.edu (D. Pompili), tmelodia@eng.buffalo.edu (T. Melodia), ian@ece.gatech.edu (I.F. Akyildiz).

1570-8705/$ - see front matter © 2008 Elsevier B.V. All rights reserved.
doi:10.1016/j.adhoc.2008.07.010

of ocean bottom sensor nodes. We propose different deployment strategies, and provide a mathematical analysis to study deployment issues concerning both architectures, with the objectives below:

- Determine the minimum number of sensors to be deployed to achieve the target sensing and communication coverage dictated by application requirements.
- Provide guidelines on how to choose the optimal deployment surface area, given a target body of water.
- Study the robustness of the sensor network to node failures, and provide an estimate of the number of redundant sensor nodes to be deployed to compensate for possible failures.

The remainder of this paper is organized as follows: in Section 2, we review related literature. In Section 3, we describe the two-dimensional and three-dimensional architectures for UW-ASNs, and discuss the relevant deployment challenges. In Section 4, we derive geometric properties of the triangular-grid deployment, evaluate the trajectory of a sinking device under the presence of ocean currents, compute the deployment surface area to deploy sensors when a 2D bottom target area needs to be covered, and provide an estimate of the number of redundant sensors to compensate for possible failures. In Section 5, we propose and compare through simulation experiments three deployment strategies for 3D UW-ASNs. Finally, in Section 6, we draw the main conclusions.

2. Related work

The problem of sensing and communication coverage for terrestrial wireless sensor networks has been addressed in several papers. However, to the best of the authors' knowledge, this work is the first to study deployment issues for underwater sensor networks. Many previous deployment solutions and theoretical bounds assuming spatio-temporal correlation, mobile sensors, redeployment of nodes, and particular deployment grid structures may not be feasible for the underwater environment.

In particular, in Ref. [9], methods for determining network connectivity and coverage given a node-reliability model are discussed, and an estimate of the minimum required node reliability for meeting a system-reliability objective is provided. An interesting result is that connectivity does not necessarily imply coverage. As the node-reliability decreases, in fact, the sufficient condition for connectivity becomes weaker than the necessary condition for coverage. Moreover, the power required by each active node for connectivity and coverage decreases at a faster rate than the rate at which the number of nodes increases. Although Ref. [9] provides useful theoretical bounds and insight into the deployment of wireless terrestrial sensor networks, the analysis is limited to grid structures.

In Ref. [3], two coordination sleep algorithms are compared, i.e., a *random* and a *coordinated sleep scheme*, in terms of two performance metrics. The first metric, the so-called *extensity*, refers to the probability that any given point is not covered, while the second metric, *intensity*, gives the tail distribution of a given point not covered for longer than a given period of time. It is shown in Ref. [3] that when the density of the network increases, the duty cycle of the network can be decreased for a fixed coverage. However, beyond a certain threshold increased redundancy in the sensor deployment does not provide same amount of reduction in the duty cycle. Although Ref. [3] provides sound coverage algorithms for terrestrial sensor networks, its results cannot be directly applied to the underwater environment where the sensor density is much lower than in the terrestrial case, and spatio-temporal correlation may often not be assumed [1]. Moreover, it is shown that coordinated sleep schedules can achieve higher duty cycle reduction at the cost of extra control overhead. Using the intensity analysis of the network, the authors propose a random sleeping schedule for a satisfactory coverage.

In Ref. [13], sensor coverage is achieved by moving sensor nodes after an initial random deployment. The algorithm assumes a cluster-based architecture and it is executed at the cluster heads. It uses virtual positive or negative forces between nodes based on their relative locations. However, although the simulation results reveal that the algorithm improves the coverage of the sensor network, [13] requires either mobile sensor nodes or redeployment of nodes, which may not be feasible for UW-ASNs.

In [7], sensing and communication coverage in a three-dimensional environment are rigorously investigated. The diameter and minimum and maximum degree of the reachability graph describing the network are derived as a function of the communication range, while different degrees of coverage (1-coverage and, more in general, k-coverage) for the 3D environment are characterized as a function of the sensing range. Interestingly, it is shown that the sensing range r required to achieve 1-coverage is greater than the transmission range t that guarantees network connectivity. Since in typical applications $t \geqslant r$, the network is guaranteed to be connected, when 1-coverage is achieved. Although these results were derived for terrestrial networks, they can also be applied in the underwater environment. Thus, in this work, we focus on the sensing coverage when discussing deployment issues in 3D UW-ASNS, as in three-dimensional networks it implicitly implies communication coverage.

3. Communication architectures

We consider two communication architectures for underwater sensor networks, i.e., a *two-dimensional* and a *three-dimensional architecture* [1], and identify the relevant deployment challenges. As in terrestrial sensor networks, in UW-ASNs it is necessary to provide *communication coverage*, i.e., all sensors should be able to establish multi-hop paths to the sink, and *sensing coverage*, i.e., the monitored body of water should be covered by the sensors. More formally, the *sensing range* r of a sensor is the radius of the sphere that models the region monitored by the sensor (sensing sphere). A portion $\mathscr{A}_\eta$ of the monitored region $\mathscr{A}$ is said to be *k-covered* if every point in $\mathscr{A}_\eta$ falls within the sensing sphere of at least k sensors. The *k-coverage ratio* η_k of a monitored region $\mathscr{A}$ is the fraction of the

Please cite this article in press as: D. Pompili et al., Three-dimensional and two-dimensional deployment analysis ..., Ad Hoc Netw. (2008), doi:10.1016/j.adhoc.2008.07.010

volume/area that is k-covered by a 3D/2D UW-ASN, respectively. In the following, we will consider the case of $k = 1$ both for 2D and 3D networks to obtain simple *1-coverage* η_1 of the region, since underwater sensors are expensive devices because of the low economy of scale caused by a small relative number of suppliers and spatio-temporal correlation may not be assumed [2].

3.1. Two-dimensional UW-ASNs

A reference architecture for two-dimensional underwater sensor networks is shown in Fig. 1, where deployed sensor nodes are anchored to the bottom of the ocean. Underwater sensors may be organized in a cluster-based architecture, and be interconnected to one or more *underwater gateways* (uw-gateways) by means of wireless acoustic links. uw-Gateways are network devices in charge of relaying data from the ocean bottom network to a surface station. They are equipped with a long-range *vertical* transceiver, which is used to relay data to a *surface station*, and with a *horizontal* transceiver, which is used to communicate with the sensor nodes to send commands and configuration data, and to collect monitored data. The surface station is equipped with an acoustic transceiver, which may be able to handle multiple parallel communications with the uw-gateways, and with a long-range radio transmitter and/or satellite transmitter, which is needed to communicate with an *onshore sink* and/or to a *surface sink*. Sensors can be connected to uw-gateways via direct links or through multi-hop paths [5]. However, in UW-ASN, the power necessary to transmit may decay with powers greater than two of the distance [10], and the uw-sink may be far from the sensor node. Consequently, although direct link connection is the simplest way to network sensors, it may not be the most energy efficient solution. Furthermore, direct links are very likely to reduce the network throughput because of increased acoustic interference due to high transmission power. In case of multi-hop paths, the data produced by a source sensor is relayed by intermediate sensors until it reaches the uw-gateway. This results in energy savings and increased network capacity, but increases the complexity of the routing functionality as well. In Ref. [12], the author assesses the bandwidth dependency on the distance using an interesting information-theoretic approach that takes into account the underwater acoustic propagation loss and ambient noise. The author defines the bandwidth corresponding to optimal signal energy allocation as the one that maximizes the channel capacity subject to the constraint that the transmission power be finite. Numerical evaluation quantifies the bandwidth and the channel capacity, as well as the transmission power needed to achieve a *pre-specified* SNR threshold, SNRth, as functions of distance.

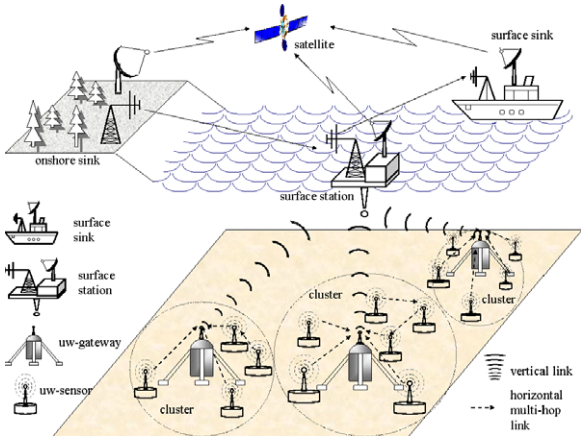

Fig. 1. Architectures for two-dimensional UW-ASNs.

3.1.1. Deployment challenges in 2D UW-ASNs

The main challenges that arise with such two-dimensional architecture are: (i) determine the minimum number of sensors and uw-gateways that need to be deployed to achieve the target sensing and communication coverage, which are dictated by the application requirements; (ii) provide guidelines on how to choose the optimal deployment surface area, given a target bottom area; and (iii) study the topology robustness of the sensor network to node failures, and provide an estimate of the number of redundant sensor nodes to be deployed to compensate for failures. In Section 4, we discuss in detail these issues and provide solutions.

3.2. Three-dimensional UW-ASNs

Three-dimensional underwater networks are used to detect and observe phenomena that cannot be adequately observed by means of ocean bottom uw-sensor nodes, i.e., to perform cooperative sampling of the 3D ocean environment. In this architecture, sensors float at different depths to observe a given phenomenon. One possible solution would be to attach each sensor node to a surface buoy, by means of wires whose length can be regulated to adjust the depth of each sensor node. However, although this solution enables easy and quick deployment of the sensor network, multiple floating buoys may obstruct ships navigating on the surface, or they can be easily detected and deactivated by enemies in military settings. Furthermore, floating buoys are vulnerable to weather and tampering or pilfering. A different approach, which was proposed for the first time in Ref. [1], is to anchor winch-based sensor devices to the bottom of the ocean, as depicted in Fig. 2. Each sensor is anchored to the ocean bottom and is equipped with a floating buoy that can be inflated by a pump. The buoy pulls the sensor towards the ocean surface. The depth of the sensor can then be regulated by adjusting the length of the wire that connects the sensor to the anchor, by means of an electronically controlled engine that resides on the sensor.

3.2.1. Deployment challenges in 3D UW-ASNs

Many challenges arise with such architecture, which need to be solved in order to enable underwater monitoring, including: (i) sensors should collaboratively regulate their depth to achieve 3D *sensing coverage* of the ocean column, according to their sensing ranges; (ii) sensors should be able to relay information to the surface station via multi-hop paths, as in 3D underwater networks there may be no notion of uw-gateway. Thus, network devices should

Please cite this article in press as: D. Pompili et al., Three-dimensional and two-dimensional deployment analysis ..., Ad Hoc Netw. (2008), doi:10.1016/j.adhoc.2008.07.010

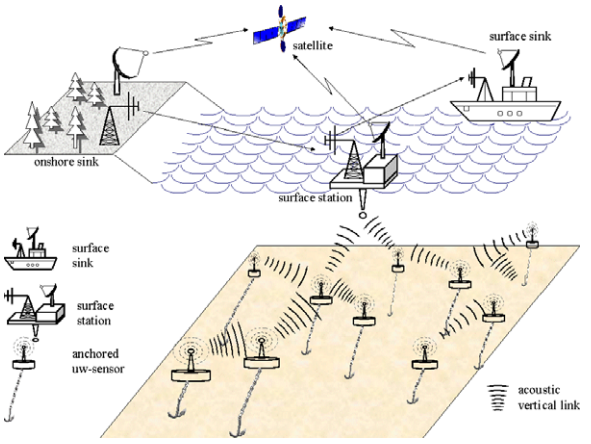

Fig. 2. Architectures for three-dimensional UW-ASNs.

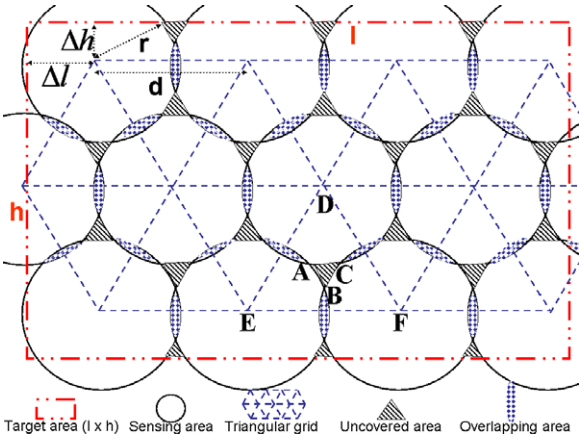

Fig. 3. Triangular-grid deployment: grid structure and side margins.

coordinate their depths in such a way as to guarantee that the network topology be always connected, i.e., at least one path from every sensor to the surface station always exists, and achieve *communication coverage*. We discuss sensing and communication coverage in 3D UW-ASNs in Section 5, and propose three deployment solutions.

4. Deployment in a 2D environment

In this section, we provide a mathematical analysis of the graph properties of sensor devices that are deployed on the surface of the ocean, sink, and reach the ocean bottom. To achieve this, we study the trajectory of sinking devices (sensors and uw-gateways) when they are deployed on the ocean surface with known initial conditions (position and velocity). This allows us to capture both the case when sensor nodes are *randomly deployed* on the ocean surface, e.g., scattered from an airplane, or the case when sensors are *accurately positioned*, e.g., released from a vessel.

To address the deployment challenges presented in the previous section, in Section 4.1 we propose the *triangular-grid* deployment, and derive useful geometric properties. In Section 4.2, we study the dynamics of a sinking object and evaluate its trajectory under the presence of ocean currents. In Section 4.3, we characterize the different sinking behavior of sensors and uw-gateways, with the objective of describing their average horizontal displacement and study the main communication properties of sensor clusters. In Section 4.4, we derive the side margins that should be used to deploy sensors on the ocean surface when a 2D target area needs to be covered on the ocean bottom under the presence of currents. Finally, in Section 4.5, we derive an estimate of the number of redundant sensors to be deployed to compensate for possible failures and provide the network with robustness.

4.1. Triangular-grid coverage properties

In this section, we propose the *triangular-grid* deployment, and derive useful geometric properties. Let us consider the common case of sensors with same sensing range r. The optimal deployment strategy to cover a two-dimensional rectangular area using the minimum number of sensors is to center each sensor at the vertex of a grid of equilateral triangles, as shown in Fig. 3. With this configuration, by adjusting the distance d among sensors, i.e., the side of the equilateral triangles, it is possible to increase the coverage (by reducing the uncovered areas), and even to achieve *full coverage*, i.e., $\eta = 1$. In addition, this enables to optimally control the coverage ratio η, defined as the ratio between the covered area and the target area.

In particular, as it is mathematically proven in the following, when $d = \sqrt{3}r$ the coverage ratio η is equal to 1, i.e., the *uncovered areas* as depicted in Figs. 3 and 4 are zero, and the *overlapping areas* are minimized. This allows to achieve the full coverage of a target area, but requires the highest number of sensors. Conversely, as the distance among sensors increases, i.e., the number of deployed sensors decreases, the coverage ratio decreases. Therefore, there is a trade-off between the number of deployed sensors and the achievable sensing coverage. We are interested in finding the minimum number of sensors that need to be deployed to guarantee a target sensing coverage η^*, which is dictated by the application requirements. To this end, we present the following theorem.

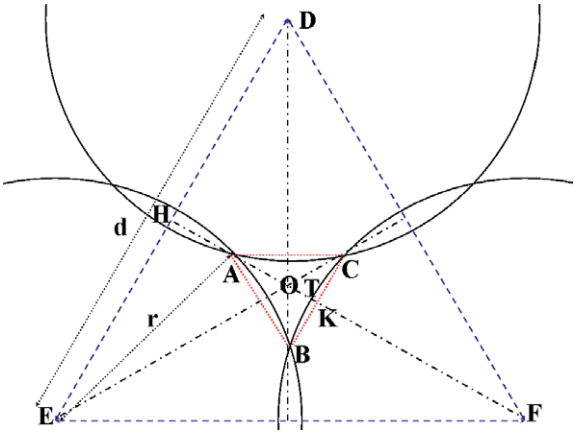

Fig. 4. Triangular-grid deployment: uncovered area (*ABC*).

Theorem 1. *In an equilateral grid the sensing coverage $\eta(d,r)$, i.e., the ratio of the total covered area and the target area, is*

$$\eta(d,r)=\eta\left(\frac{d}{r}\right)=\begin{cases}\dfrac{\mathscr{A}_{DEF}-\mathscr{A}_{ABC}}{\mathscr{A}_{DEF}}=1-\dfrac{\mathscr{A}_{ABC}}{\frac{\sqrt{3}}{4}d^2} & \dfrac{d}{r}\in[0,2]\\ \dfrac{3\cdot\frac{\pi r^2}{6}}{\frac{\sqrt{3}}{4}d^2}=\dfrac{2\pi}{\sqrt{3}}\cdot\left(\dfrac{d}{r}\right)^{-2} & \dfrac{d}{r}\in(2,\infty),\end{cases} \tag{1}$$

where

$$\mathscr{A}_{ABC}=\tfrac{\sqrt{3}}{4}\left(\tfrac{d}{2}-\sqrt{3r^2-\tfrac{3}{4}d^2}\right)^2-3r^2\arcsin\tfrac{\overline{BC}}{2r}+ \\ +\tfrac{3}{4}\overline{BC}\sqrt{4r^2-\overline{BC}^2},\qquad \overline{BC}=\tfrac{d}{2}-\sqrt{3r^2-\tfrac{3}{4}d^2}. \tag{2}$$

Proof. With reference to Fig. 4, which represents a zoomed portion of Fig. 3, $\overline{AE}=r$ and $\overline{EH}=d/2$, where r is the sensing range and d is the distance between sensors. Since the triangle *DEF* is equilateral by construction, $\overline{HO}=(\sqrt{3}/6)d$. Consequently, since $\overline{AH}=\sqrt{r^2-d^2/4}$, it holds that $\overline{AO}=\overline{HO}-\overline{AH}=(\sqrt{3}/6)d-\sqrt{r^2-d^2/4}$. Since triangle *DEF* is equilateral, triangle *ABC* is equilateral too. Consequently, as $\overline{AO}=(\sqrt{3}/3)\overline{BC}$, then $\overline{BC}=d/2-\sqrt{3r^2-(3/4)d^2}$. Therefore, the area of triangle *ABC* is $\mathscr{A}^{\triangle}_{ABC}=(\sqrt{3}/4)\overline{BC}^2$. In order to express the sensing coverage $\eta(d,r)$ as a function of d and r, we need to compute the area $\mathscr{A}_{ABC}$ of the uncovered region *ABC* among the circles with centers in *D*, *E*, and *F*, and radius r. This can be computed as $\mathscr{A}_{ABC}=\mathscr{A}^{\triangle}_{ABC}-3\cdot\mathscr{A}_{BTCK}$, where $\mathscr{A}_{BTCK}$ coincides with the difference of the areas of the circular sector *BTCF* and the triangle *BCF*, i.e., $\mathscr{A}_{BTCK}=\mathscr{A}_{BTCF}-\mathscr{A}^{\triangle}_{BCF}=r^2\arcsin(\overline{BC}/2r)-(\overline{BC}/4)\sqrt{4r^2-\overline{BC}^2}$. Consequently, $\mathscr{A}_{ABC}=(\sqrt{3}/4)(d/2-\sqrt{3r^2-(3/4)d^2})^2-3r^2\arcsin(\overline{BC}/2r)+(3/4)\overline{BC}\sqrt{4r^2-\overline{BC}^2}$, where $\overline{BC}=d/2-\sqrt{3r^2-(3/4)d^2}$, which gives Eq. (1) in the non-trivial case $d/r\in[0,2]$. As far as the case $d/r\in(2,\infty)$ is concerned, no overlapping areas are formed, and the coverage η can be computed straightforward. □

Corollary 1. *In an equilateral grid the sensing coverage depends only on the ratio of the inter-sensor distance d and the sensing range r, and not on their absolute values, i.e., $\eta(d,r)=\eta(d/r)$.*

Let us note in Eq. (1) that, when $d/r\leqslant\sqrt{3}$, it holds $\mathscr{A}^{\triangle}_{ABC}=\mathscr{A}_{ABC}=0$, which means that in this case the highest possible coverage is achieved ($\eta=1$). Moreover, $\mathscr{A}_{ABC}(d)$ is a monotonically increasing function when d/r ranges in $[\sqrt{3},2]$, which makes the coverage $\eta(d,r)$ a monotonically decreasing function when $d/r>\sqrt{3}$. Fig. 5 reports the sensing coverage as a decreasing function of the ratio of d and r. For a target sensing coverage $\eta^*=0.95$, it is shown that the optimal ratio is $d^*/r=1.95$.

In order to compute the minimum number of sensors that need to be deployed to cover a target area with sides l and h using the proposed equilateral grid, we should first find the optimal *margins* Δl and Δh from the center of the upper-left sensing circle, as shown in Fig. 3. In particular, given the application-dependent target coverage η^*, from

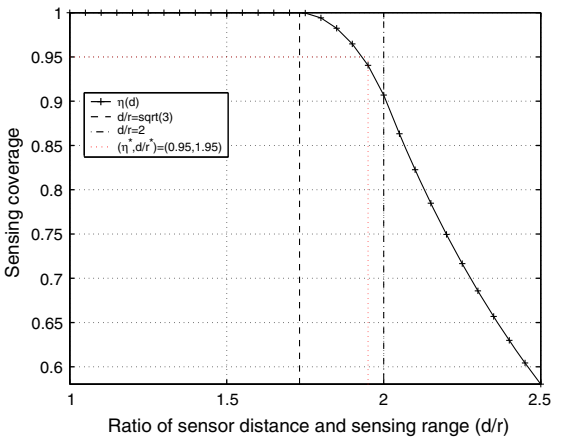

Fig. 5. Triangular-grid deployment: sensing coverage.

Fig. 5 we compute the optimal ratio d^*/r. In order for the regions at the border of the target area to have the same coverage ratio η^* than inner regions, the margins should be selected as $\Delta h=\overline{HO}+\overline{OT}=(\sqrt{3}/2)d^*-r$, where $\overline{OT}=\overline{OF}-\overline{TF}=(\sqrt{3}/3)d-r$, and $\Delta l=2\overline{OH}\cos(\pi/6)=d^*/2$. If we denote N^* as the minimum number of sensors, we have $N^*=N^*_l\cdot N^*_h$, where N^*_l and N^*_h represent the minimum number of sensors deployed along sides l and h, respectively. Consequently, to properly cover the entire target area, the following relations need to be satisfied

$$2\Delta l+(N^*_l-1)d^*\geqslant l\Rightarrow N^*_l=\left\lceil\frac{l-d^*}{d^*}+1\right\rceil$$

$$2\Delta h+(N^*_h-1)d^*\sin(\pi/6)\geqslant h\Rightarrow N^*_h=\left\lceil\frac{2\sqrt{3}h-6d^*+4\sqrt{3}r}{3d^*}+1\right\rceil.$$

Finally, the minimum number of sensors N^* required to cover a target area with sides l and h, under the constraints of providing a ratio d^*/r to satisfy the target coverage ratio η^* is

$$N^*(l,h,d^*,r)=\left\lceil\frac{l-d^*}{d^*}+1\right\rceil \\ \cdot\left\lceil\frac{2\sqrt{3}h-6d^*+4\sqrt{3}r}{3d^*}+1\right\rceil. \tag{3}$$

In Figs. 6–8, (3) is plotted for three different target areas, i.e., $A_1=100\times100\ \mathrm{m}^2$, $A_2=300\times200\ \mathrm{m}^2$, and $A_3=1000\times1000\ \mathrm{m}^2$, and for several sensing ranges r in the interval [10,35] m.

4.2. Trajectory of a sinking object

In this section, we study the dynamics of a sinking object and evaluate its trajectory under the presence of ocean currents. In particular, we first consider the ideal case in which the velocity of the ocean current does not change with depth; then, we extend the model to capture the more realistic case in which the velocity of the current depends on depth.

According to Newton's first law of motion, the acceleration $\vec{\mathbf{a}}$ describing the sinking in the water of an object with a density ρ and volume V is determined by the following vectorial motion law

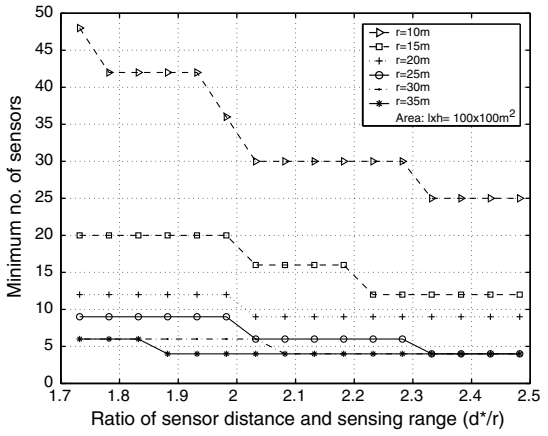

Fig. 6. Minimum number of sensors in triangular-grid deployment vs. sensor distance over sensing range ($A_1 = 100 \times 100\ \mathrm{m}^2$).

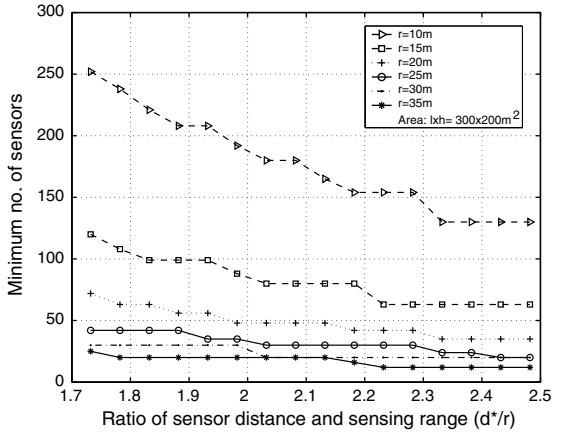

Fig. 7. Minimum number of sensors in triangular-grid deployment vs. sensor distance over sensing range ($A_1 = 300 \times 200\ \mathrm{m}^2$).

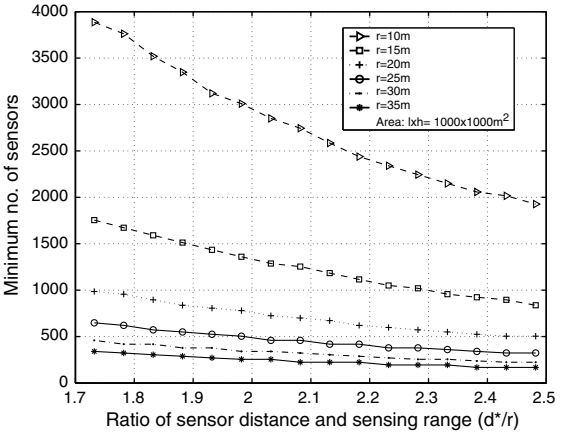

Fig. 8. Minimum number of sensors in triangular-grid deployment vs. sensor distance over sensing range ($A_1 = 1000 \times 1000\ \mathrm{m}^2$).

$$\vec{\mathbf{F}}_{\mathbf{W}} + \vec{\mathbf{F}}_{\mathbf{B}} + \vec{\mathbf{F}}_{\mathbf{R}} + \vec{\mathbf{F}}_{\mathbf{C}} = \rho V \cdot \vec{\mathbf{a}}, \tag{4}$$

where $\vec{\mathbf{F}}_{\mathbf{W}} = \rho V \cdot \vec{\mathbf{g}}$ is the *weight force*, which depends on the density ρ (kg/m^3) and volume V (m^3) of the sinking object, and on the terrestrial gravitational acceleration $g = 9.81$ m/s^2; $\vec{\mathbf{F}}_{\mathbf{B}} = -\rho_w V \cdot \vec{\mathbf{g}}$ is the *buoyant force* due to the Archimede's principle, which is equal to the weight of the displaced fluid, where $\rho_w = 1050$ kg/m^3 represents the average density of salty water; $\vec{\mathbf{F}}_{\mathbf{R}} = -K\rho_w \mu A_R \cdot \vec{\mathbf{v}}$ is the *fluid resistance force*, which is proportional through the constant $K = 0.2$ Nm^{2}s/kg [8] to the velocity $\vec{\mathbf{v}}$ (m/s) of the object, to its cross-section A_R (m^2), and to a parameter μ accounting for the resistance caused by the object shape; $\vec{\mathbf{F}}_{\mathbf{C}} = C\sigma A_C \cdot (\vec{\mathbf{v}}_{\mathbf{c}} - \vec{\mathbf{v}})$ is the *force of the current*, which is proportional through the constant $C = 721.7$ Ns/m^3 [8] to the difference between the velocity of the ocean current $\vec{\mathbf{v}}_{\mathbf{c}}$ (m/s) and the object velocity $\vec{\mathbf{v}}$ (m/s), to the cross-section A_C (m^2) of the object facing the current, and to an object-dependent shape factor σ.

4.2.1. Ideal one-layer current

Let us start considering the ideal case where the velocity of the current $\vec{\mathbf{v}}_{\mathbf{c}} = (v_c^x, v_c^y, v_c^z)$ is assumed to be independent on the ocean depth (we will then relax this assumption). Under the assumption that no significant vertical movement of ocean water is observed, i.e., the considered area is neither an *upwelling* nor a *downwelling area*, the current along the z-axes can be neglected ($v_c^z \approx 0$), and Eq. (4) leads to three scalar laws

$$x : F_C^x = \rho V \ddot{x}; \quad y : F_C^y = \rho V \ddot{y}; \quad z : F_W^z + F_B^z + F_R^z = \rho V \ddot{z}, \tag{5}$$

where we projected Eq. (4) onto the x-, y-, and z- axes, which are directed as shown in Fig. 9, and we denoted the dynamic position of the sinking object as $\mathbf{P} = (x, y, z)$, its velocity as $\vec{\mathbf{v}} = (\dot{x}, \dot{y}, \dot{z})$, and its acceleration as $\vec{\mathbf{a}} = (\ddot{x}, \ddot{y}, \ddot{z})$.

Specifically, we obtain the following dynamic system equations

$$\begin{cases} \ddot{x} + \dfrac{C\sigma A^{xy}}{\rho V}\dot{x} = \dfrac{C\sigma A^{xy}}{\rho V} v_c^x \\ \ddot{y} + \dfrac{C\sigma A^{xy}}{\rho V}\dot{y} = \dfrac{C\sigma A^{xy}}{\rho V} v_c^y \\ \ddot{z} + \dfrac{K\mu\rho_w A^z}{\rho V}\dot{z} = g\dfrac{\rho - \rho_w}{\rho}, \end{cases} \tag{6}$$

where A^{xy} and A^z represent the horizontal and vertical cross-sections, respectively. By solving this dynamic system, with the initial conditions of the object on the surface at time t^0, i.e., its position $\mathbf{P}(t^0) = (x(t^0), y(t^0), 0)$ and velocity $\vec{\mathbf{v}}(t^0) = (\dot{x}(t^0), \dot{y}(t^0), \dot{z}(t^0))$, we obtain the solution

$$\begin{cases} x(t) = x(t^0) + v_c^x \cdot (t - t^0) + \dfrac{\dot{x}(t^0) - v_c^x}{C\sigma A^{xy}/\rho V} \cdot \left[1 - \mathrm{e}^{-\frac{C\sigma A^{xy}}{\rho V}\cdot(t-t^0)}\right] \\ y(t) = y(t^0) + v_c^y \cdot (t - t^0) + \dfrac{\dot{y}(t^0) - v_c^y}{C\sigma A^{xy}/\rho V} \cdot \left[1 - \mathrm{e}^{-\frac{C\sigma A^{xy}}{\rho V}\cdot(t-t^0)}\right] \\ z(t) = v_\infty^z \cdot (t - t^0) + [\dot{z}(t^0) - v_\infty^z] \cdot \left[1 - \mathrm{e}^{-\frac{K\rho_W \mu A^z}{\rho V}\cdot(t-t^0)}\right], \end{cases} \tag{7}$$

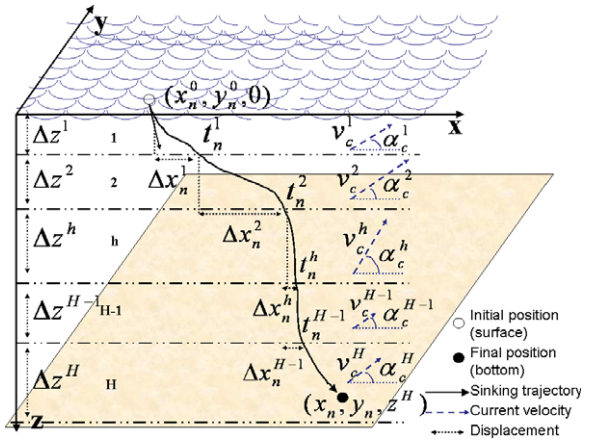

Fig. 9. Trajectory of a sinking object.

where we denoted as $v^z_\infty = gV(\rho - \rho_w)/K\rho_w\mu A^z$ (m/s) the *terminal velocity* along z, which is computed by imposing in Eq. (5) the following force equilibrium, $F^z_W + F^z_B + F^z_R = 0$, i.e., $\ddot{z} = 0$ in Eq. (6). Note that the parameter $\rho V/C\sigma A^{xy}$ (s) in the argument of the exponential in Eq. (7) is the *time constant* of the differential equation solution, and represents the *inertial* parameter of the system, i.e., when $t - t^0 > 5 \cdot \rho V/C\sigma A^{xy}$ then the velocity $\mathbf{v}$ of the object differs from the current velocity $\mathbf{v_c}$ by less than 1%.

4.2.2. Multi-layer current

Let us now generalize this result by considering the more realistic case in which the velocity of the ocean current depends on depth, i.e., $\vec{\mathbf{v}}_\mathbf{c} = (v^x_c(z), v^y_c(z), 0)$. There are two types of marine currents each caused by a range of distinct drivers, *non tidal* ocean currents, such as the Gulf Stream, and *tidal* streams. The complex hydrodynamic system of currents is powered by many forces, the crux being the playoff between the joint forces of solar heating of tropical surface waters and the polar contributions of cold fresh water ice-melt flooding into the ocean and the general cooling of the salty ocean water. While studying the global current systems makes up the larger part of the science of *oceanography*, in this paper we focus on the effect of *local streams* in the monitored volume region. In particular, we consider an ocean volume with constant depth z^H (*flat bottom*), and H different ocean current layers $h = 1, \ldots, H$, of width Δz^h. We model the current on each plane xy in a layer h to be a piecewise constant function with module v^h_c and angular deviation from the x-axes α^h_c, as depicted in Fig. 9. This allows us to model the *thermohaline circulation* (also known as the ocean's conveyor belt), i.e., deep ocean current, sometimes called *submarine rivers*, that flows with constant velocity and direction within certain depths, driven by density and temperature gradients.

Given these assumptions, our objective is to calculate the horizontal displacement of a sinking object on the x- and y-axes in each of the layers it sinks through. To accomplish this, we recursively apply the solution (7) to the dynamic system (6) in each current layer, using as initial conditions of the object the final position and velocity computed in the previous layer. If we denote the initial position of object n as $(x^0_n, y^0_n, 0)$ and its velocity as $(\dot{x}^0_n, \dot{y}^0_n, \dot{z}^0_n)$, given all its physical characteristics such as volume V_n, density ρ_n, cross-sections A^{xy}_n and A^z_n, and horizontal and vertical shape factors, μ_n and σ_n, respectively, we can track the position of n while it sinks. Specifically, we have

$$\begin{cases} x_n(t) = x^0_n + \sum_{i=1}^{h-1} \Delta x^i_n + v^h_c \cos\alpha^h_c \cdot (t - t^{h-1}_n) + \\ \quad + \dfrac{\dot{x}_n(t^{h-1}_n) - v^h_c \cos\alpha^h_c}{C\sigma_n A^{xy}_n/\rho_n V_n} \cdot \left[1 - \mathrm{e}^{-\frac{C\sigma_n A^{xy}_n}{\rho_n V_n}(t - t^{h-1}_n)}\right] \\ y_n(t) = y^0_n + \sum_{i=1}^{h-1} \Delta y^i_n + v^h_c \sin\alpha^h_c \cdot (t - t^{h-1}_n) + \\ \quad + \dfrac{\dot{y}_n(t^{h-1}_n) - v^h_c \sin\alpha^h_c}{C\sigma_n A^{xy}_n/\rho_n V_n} \cdot \left[1 - \mathrm{e}^{-\frac{C\sigma_n A^{xy}_n}{\rho_n V_n}(t - t^{h-1}_n)}\right] \\ z_n(t) = \min\{v^z_{\infty n} \cdot (t - t^0_n) + \\ \quad + [\dot{z}^0_n - v^z_{\infty n}] \cdot \left[1 - \mathrm{e}^{-\frac{K\rho_W \mu_n A^z_n}{\rho_n V_n}(t - t^0_n)}\right]; z^H\}, \\ t^{h-1}_n \leqslant t \leqslant t^h_n, \end{cases} \tag{8}$$

where t^0_n and t^h_n are the instants object n is released on the ocean surface and exits layer h, respectively. More precisely, t^h_n is the instant for which it holds $z_n(t^h_n) = z^h = \sum_{i=1}^h \Delta z^i$, i.e., the depth of the object coincides with the sum of the width Δz^i of each layer i the object sank through, as shown in Fig. 9.

In Eq. (8), the instantaneous total displacement on the x- and y-axes when the sinking object is inside layer h is *recursively* computed as the sum of the displacements in each of the $h-1$ previously crossed layers $i = 1, \ldots, h-1$, plus the displacement in layer h itself. These displacements are determined as partial solution of the dynamic system (6) in each layer, and have the following structure,

$$\begin{cases} \Delta x^i_n = v^i_c \cos\alpha^i_c \cdot (t^i_n - t^{i-1}_n) + \\ \quad + \dfrac{\dot{x}_n(t^{h-1}_n) - v^h_c \cos\alpha^h_c}{C\sigma_n A^{xy}_n/\rho_n V_n} \cdot \left[1 - \mathrm{e}^{-\frac{C\sigma_n A^{xy}_n}{\rho_n V_n}(t^i_n - t^{i-1}_n)}\right] \\ \Delta y^i_n = v^i_c \sin\alpha^i_c \cdot (t^i_n - t^{i-1}_n) + \\ \quad + \dfrac{\dot{y}_n(t^{h-1}_n) - v^h_c \sin\alpha^h_c}{C\sigma_n A^{xy}_n/\rho_n V_n} \cdot \left[1 - \mathrm{e}^{-\frac{C\sigma_n A^{xy}_n}{\rho_n V_n}(t^i_n - t^{i-1}_n)}\right]. \end{cases} \tag{9}$$

Finally, in order to be able to determine the position of object n from Eq. (8), we need to substitute in Eqs. (8) and (9) the x- and y-component of the velocity the object has when it enters layer $h = 1, \ldots, H$, i.e., $(\dot{x}_n(t^{h-1}_n), \dot{y}_n(t^{h-1}_n))$, which can be computed as exit velocity from layer $h-1$ by solving Eq. (6). We report these velocities in the following

$$\begin{cases} \dot{x}_n(t^{h-1}_n) = v^{h-1}_c \cos\alpha^{h-1}_c + \\ + \left[\dot{x}_n(t^{h-2}_n) - v^{h-1}_c \cos\alpha^{h-1}_c\right] \cdot \mathrm{e}^{-\frac{C\sigma_n A^{xy}_n}{\rho_n V_n}(t^{h-1}_n - t^{h-2}_n)} \\ \dot{y}_n(t^{h-1}_n) = v^{h-1}_c \sin\alpha^{h-1}_c + \\ + \left[\dot{y}_n(t^{h-2}_n) - v^{h-1}_c \sin\alpha^{h-1}_c\right] \cdot \mathrm{e}^{-\frac{C\sigma_n A^{xy}_n}{\rho_n V_n}(t^{h-1}_n - t^{h-2}_n)} \end{cases} \tag{10}$$

which can be recursively computed given that $\dot{x}_n(t^0_n)$ and $\dot{y}_n(t^0_n)$ are the known initial velocities on the surface.

Eqs. (8)–(10) allow us to track the dynamic position of object n while it sinks, given complete knowledge about the structure of the currents in the volume of interest. In practice, however, we may only leverage some statistical

information on the ocean currents, which can be used to estimate the final position of a deployed object. While this offers a mathematical tool to study the dynamic of a sinking object, our ultimate objective is to be able to infer the statistical sensing and communication properties of a two-dimensional sensor network that reaches the ocean bottom, as will be discussed in the following section.

4.3. Communication properties of 2D UW-ASNs

In this section, we characterize the different sinking behavior of sensors and uw-gateways, with the objective of describing: (i) the average horizontal displacement of sensors and uw-gateways when different depths and current velocities are considered; (ii) the main networking properties of the clusters that have an uw-gateway as cluster head, e.g., study the maximum and average sensor-gateway distance when the number of deployed gateways varies; and (iii) the average and standard deviation of number of sensors in each cluster.

Let us consider a set of sensors $\mathscr{S}$ with cardinality $S = |\mathscr{S}|$ characterized by the same density $\rho_{\mathscr{S}}$, volume V_S, cross-sections $A^{xy}_{\mathscr{S}}$ and $A^{z}_{\mathscr{S}}$, and shape factors $\mu_{\mathscr{S}}$ and $\sigma_{\mathscr{S}}$, and a set of uw-gateways $\mathscr{G}$ with $G = |\mathscr{G}|$, in general with different values of $\rho_{\mathscr{g}}$, $V_{\mathscr{g}}$, $A^{xy}_{\mathscr{g}}$, $A^{z}_{\mathscr{g}}$, $\mu_{\mathscr{g}}$, and $\sigma_{\mathscr{g}}$. Given the matrices of the known initial positions of the deployed sensors and uw-gateways, $\mathbf{P^0_{\mathscr{S}}} = [\mathbf{P^0_1}|\cdots|\mathbf{P^0_s}|\cdots|\mathbf{P^0_S}]^T$ and $\mathbf{P^0_{\mathscr{g}}} = [\mathbf{P^0_1}|\cdots|\mathbf{P^0_g}|\cdots|\mathbf{P^0_G}]^T$, respectively, where $\mathbf{P^0_s} = [x^0_s y^0_s\ 0]^T$ $\forall s \in \mathscr{S}$ and $\mathbf{P^0_g} = [x^0_g y^0_g\ 0]^T$ $\forall g \in \mathscr{G}$ are position column vectors, and the matrices of their known initial velocities, $\underline{\mathbf{v^0_{\mathscr{S}}}} = [\mathbf{v^0_1}|\cdots|\mathbf{v^0_s}|\cdots|\mathbf{v^0_S}]^T$ and $\underline{\mathbf{v^0_{\mathscr{g}}}} = [\mathbf{v^0_1}|\cdots|\mathbf{v^0_g}|\cdots|\mathbf{v^0_G}]^T$, where $\mathbf{v^0_s} = [\dot{x}^0_s \dot{y}^0_s \dot{z}^0_s]^T$ $\forall s \in \mathscr{S}$ and $\mathbf{v^0_g} = [\dot{x}^0_g \dot{y}^0_g \dot{z}^0_g]^T \forall g \in \mathscr{G}$ are velocity column vectors, the final positions on the ocean bottom of the sensors and uw-gateways, $\mathbf{P^f_{\mathscr{S}}}$ and $\mathbf{P^f_{\mathscr{g}}}$, respectively, can be derived using Eqs. (8)–(10) when all deployed devices have reached the bottom, i.e., when $t = t^f \geqslant \max\{\max_{s\in\mathscr{S}} t^H_s; \max_{g\in\mathscr{G}} t^H_g\}$. Specifically

$$\mathbf{P^f_{\mathscr{S}}} = \mathbf{P^0_{\mathscr{S}}} + \underline{\Delta\mathbf{P}_{\mathscr{S}}}(\mathbf{v^0_{\mathscr{S}}}), \quad \mathbf{P^f_{\mathscr{g}}} = \mathbf{P^0_{\mathscr{g}}} + \underline{\Delta\mathbf{P}_{\mathscr{g}}}(\mathbf{v^0_{\mathscr{g}}}), \tag{11}$$

where $\Delta\mathbf{P}_{\mathscr{S}}(\mathbf{v^0_{\mathscr{S}}})$ and $\Delta\mathbf{P}_{\mathscr{g}}(\mathbf{v^0_{\mathscr{g}}})$ are matrices accounting for the total displacements accumulated while the sensors and uw-gateways, respectively, were sinking through the ocean current layers, i.e.

$$\underline{\Delta\mathbf{P}_{\mathscr{S}}} = \begin{bmatrix} . & \sum_{h=1}^{H} \Delta x^h_s & . \\ . & \sum_{h=1}^{H} \Delta y^h_s & . \\ . & z^H & . \end{bmatrix}^T, \quad \underline{\Delta\mathbf{P}_{\mathscr{g}}} = \begin{bmatrix} . & \sum_{h=1}^{H} \Delta x^h_g & . \\ . & \sum_{h=1}^{H} \Delta y^h_g & . \\ . & z^H & . \end{bmatrix}^T. \tag{12}$$

In Eq. (12), each element can be computed as in Eq. (9). Note that the dependence on the initial velocity in Eq. (12) has been omitted for the sake of notation simplicity.

In Fig. 10, we show the expected horizontal displacement $\Delta d = \sqrt{\Delta x^2 + \Delta y^2}$ of sensors and uw-gateways when different depths and current velocities are considered. In particular, we consider $\rho_s = 2000\ \mathrm{kg/m^3}$, $\rho_g = 2500\ \mathrm{kg/m^3}$, $V_s = 0.5 \times 10^{-3}\ \mathrm{m^3}$, and $V_g = 10^{-3}\ \mathrm{m^3}$ to account for the common physical characteristics of underwater

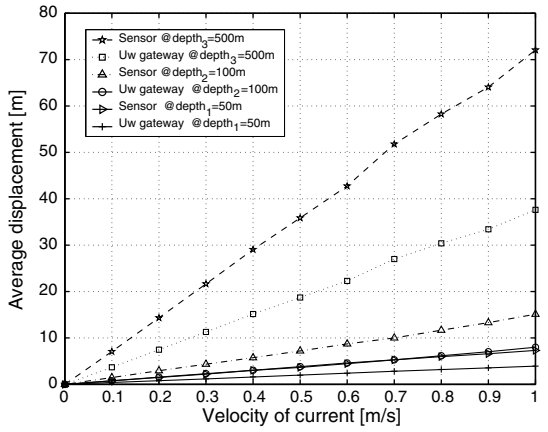

Fig. 10. Average horizontal displacement of sensors and uw-gateways vs. current velocity (for three different depths).

sensor nodes and uw-gateways, which reflect into different sinking properties, as formalized in Eq. (11). Note that gateways accumulate smaller displacements than sensors since their sinking times are shorter due to their higher weight ($\rho_g \cdot V_g > \rho_s \cdot V_s$).

In Fig. 11, we depict the maximum and average sensor-gateway distance when the number of deployed gateways increases. In particular, we consider three deployment volumes ($V_1 = 100 \times 100 \times 50\ \mathrm{m^3}$, $V_2 = 300 \times 200 \times 100\ \mathrm{m^3}$, and $V_3 = 1000 \times 1000 \times 500\ \mathrm{m^3}$) and a one-layer current scenario ($H = 1$) with $v_c^{\max} = 1\ \mathrm{m/s}$. According to the application-specific sensor transmission range t, Fig. 11 allows setting the minimum number of uw-gateways that need to be deployed. For example, in order for a sensor to be able to directly send packets to its associated uw-gateway, the maximum sensor-gateway distance should be smaller than the sensor transmission range t.

In Fig. 12, we present the normalized average and standard deviation of number of sensors per uw-gateway when two deployment strategies are considered, the *random* and the *grid deployment*. Interestingly, while the average number of sensors does not depend on the deployment strategy, the sensor dispersion is much lower in a grid structure,

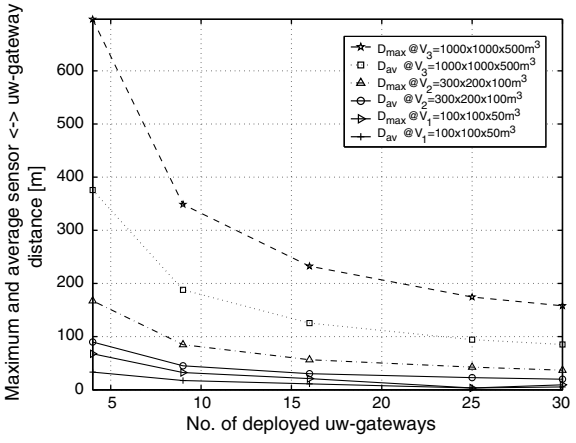

Fig. 11. Maximum and average sensor-gateway distance vs. no. of deployed gateways (in three different volumes, and with $v_c^{\max} = 1\ \mathrm{m/s}$).

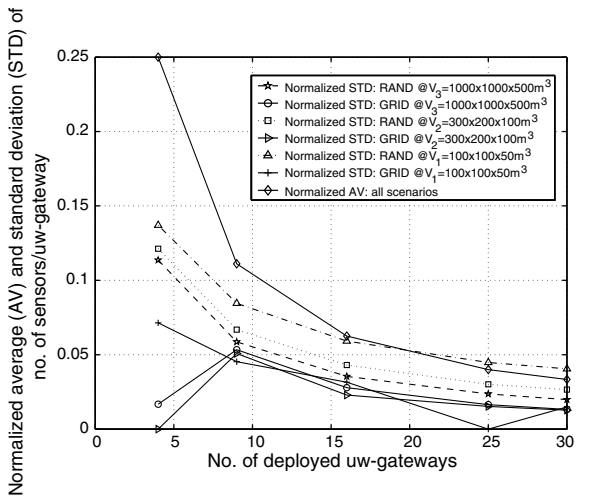

Fig. 12. Normalized average and standard deviation of number of sensors per uw-gateway vs. numbre of deployed gateways (for grid and random deployment strategies, in three different volumes, and with $v_c^{\max} = 1$ m/s).

independently on the number of gateways deployed. This is a general result that depends on the regular structure of grids, and not on the specific considered scenario.

4.4. Deployment surface area: Side margins

In this section, we compute the deployment surface area where sensors should be deployed, when a 2D target area needs to be covered on the bottom of the ocean. As described in Sections 4.2 and 4.3, ocean currents may significantly modify the sinking trajectories of sensors and uw-gateways. Therefore, the surface deployment should take the effect of the currents into account, in order to position as many deployed sensors inside the target area as possible. To achieve this, in the following we consider a *worst-case scenario* where the effect of currents, in terms of sensor displacements, is captured. The objective is to dimension the deployment surface area, i.e., to asses proper *surface side margins*.

With reference to Fig. 13, we consider a bottom target area with sides l and h, and analyze the two cases of *unknown current direction* (a), where we denote as $\Delta d_{\max} = \sqrt{\Delta x_{\max}^2 + \Delta y_{\max}^2}$ the maximum horizontal displacement a sinking sensor can experience, i.e., how far in the horizontal plane xy a sensor can drift (see Fig. 9), and *known current direction* (b), where we denote as $\Delta d_{\max}$ the same metric used in the previous case and as $\Delta\alpha_{\max}$ the maximum angular deviation of the current from its known direction β, which is the angle the direction of the current forms with side h of the target area, as depicted in Fig. 13b. Note that, without loss in generality, it always holds that $\beta \in [0, \pi/2]$. More specifically, the dotted *circular sector* in Fig. 13b, characterized by radius $\Delta d_{\max}$ and angle $2\Delta\alpha_{\max}$, represents the region of the ocean bottom that may be reached by a sensor that is deployed on the ocean surface exactly on the vertex of the circular sector itself. This region represents the statistical uncertainty in the final anchor position of a sensor caused by drifting due to ocean currents during the sinking.

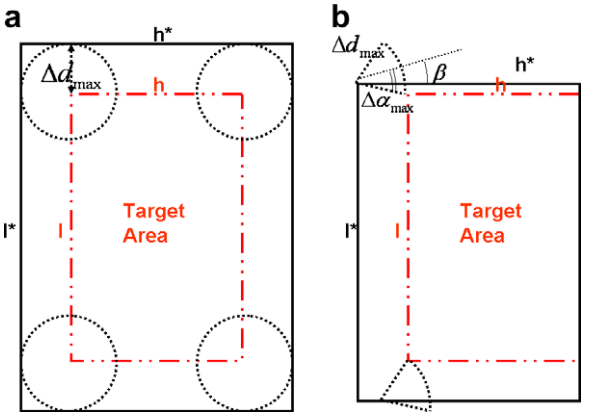

Fig. 13. Deployment surface area for unknown (a) and known (b) current direction β, given a bottom target area $l \times h$.

As far as the side margins in the unknown current direction case are concerned, from geometric properties of Fig. 13a it holds

$$\begin{cases} l^* = l + 2\Delta d_{\max} \\ h^* = h + 2\Delta d_{\max}, \end{cases} \tag{13}$$

while for the known current direction case (Fig. 13b) it can be proven with simple trigonometry derivations that it holds

$$\begin{cases} l^* = l + \Delta d_{\max} \cdot \{\max[0; \sin(\beta - \Delta\alpha_{\max})] + \sin(\beta + \Delta\alpha_{\max})\} \\ h^* = h + \Delta d_{\max} \cdot \{\max[\cos(\beta - \Delta\alpha_{\max}); \cos(\beta + \Delta\alpha_{\max})]\}. \end{cases} \tag{14}$$

In Eqs. (13) and (14), the worst-case maximum displacement and maximum angular deviation a sensor can experience are

$$\Delta d_{\max} = \overline{OA_H} = \frac{z^H}{\cos(\Delta\alpha_{\max})} \tag{15}$$

$$\Delta\alpha_{\max} = \arctan \frac{\sum_{h=1}^{H} v_c^{h,\max} \Delta z^h \sin \alpha_c^{h,\max}}{\sum_{h=1}^{H} v_c^{h,\max} \Delta z^h \cos \alpha_c^{h,\max}}, \tag{16}$$

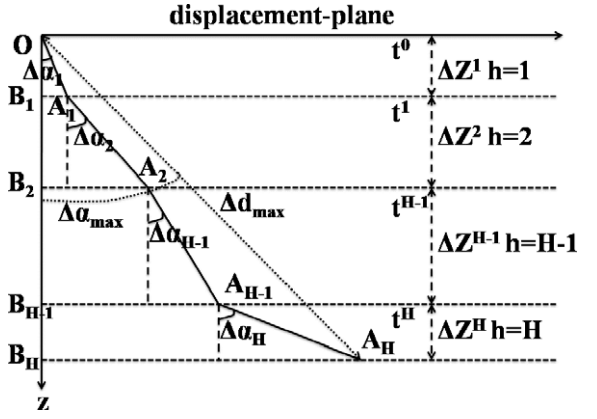

Fig. 14. Displacement-plane vs. depth.

where z^H is the ocean depth, H is the number of ocean current layers, Δz^h is the width of layer h, and $v_c^{h,max}$ and $\alpha_c^{h,max}$ are the maximum current velocity and angular deviation in layer h, respectively. The mathematical derivation of Eqs. (15) and (16) are reported in the following.

With reference to Fig. 14, it holds that

$$\tan(\Delta\alpha_{\max}) = \frac{\overline{A_H B_H}}{\overline{OB_H}} = \frac{\overline{OA_1}\sin(\Delta\alpha_1) + \overline{A_1A_2}\sin(\Delta\alpha_2) + \cdots + \overline{A_{h-1}A_h}\sin(\Delta\alpha_h) + \cdots + \overline{A_{H-1}A_H}\sin(\Delta\alpha_H)}{\overline{OA_1}\cos(\Delta\alpha_1) + \overline{A_1A_2}\cos(\Delta\alpha_2) + \cdots + \overline{A_{h-1}A_h}\cos(\Delta\alpha_h) + \cdots + \overline{A_{H-1}A_H}\cos(\Delta\alpha_H)}. \quad (17)$$

If we assume that the vertical velocity of the sinking object is constant and equal to v_∞^z (i.e., the object terminal velocity as described in Section 4.2), then the time for an object to sink through the generic layer h will be $\Delta t^h = t^h - t^{h-1} = \Delta z^h / v_\infty^z$. Therefore, in (17), it holds that $\overline{OA_1} = v_c^{1,max} \cdot \Delta z^1 / v_\infty^z$ and $\overline{A_{h-1}A_h} = v_c^{h,max} \cdot \Delta z^h / v_\infty^z$. This leads to Eq. (16) if we simplify the terminal velocity both in the numerator and the denominator. Finally, Eq. (15) can be derived by trivial trigonometric derivations.

Interestingly, given the same target area, the side surface margins in the unknown current direction case (13) are larger than those computed if some information about the current direction can be leveraged Eq. (14). This is also shown in Fig. 13, where the surface areas (outside solid rectangles) in the two cases are noticeably different, while the target area (inside dotted rectangle) is the same.

4.5. Reliability margin

In this section, we provide an estimate of the number of redundant sensors required to provide the network with robustness to node failures, which underwater may be caused by fouling and corrosion. In particular, we study the required topology redundancy to statistically compensate for node failures within a pre-determined observation period, i.e., the length of the monitoring mission. If we assume all nodes to have the same failure rate, and node failures to be independent and occurring according to a Poisson distribution, the minimum number of redundant sensors ΔN^* to be deployed to compensate for Poissonian sensor failures is

$$\sum_{n=0}^{\Delta N^*} \frac{(\lambda T)^n \cdot e^{-\lambda T}}{n!} \geqslant \Gamma^*, \quad (18)$$

where λ (day^{-1}) represents the sensor failure rate, T (day) the observation time, n the number of sensors that experience a failure within the observation time, and Γ^* the target success probability, i.e., the probability that no more than ΔN^* failures be experienced during the observation time.

Given a fixed number of redundant sensors deployed in the body of water, which we indicated as ΔN^*, the left side of Eq. (18) computes the probability of having no network failures in the observation time T, i.e., no more than ΔN^* single sensor failures. For example, if $\Delta N = 0^*$, only the strictly necessary number of sensors are deployed, without considering any margin (i.e., the network cannot bear any single sensor failure). In this case, the left side of Eq. (18) reduces to $e^{-\lambda T}$, which represents the success probability of one sensor, i.e., the probability that a single sensor does not experience a failure in the monitoring time window. In this scenario, which represents *the lowest degree of network robustness to node failures*, this probability decreases as the observation time T increases, and depends on the reliability of each single sensor (that is determined by the sensor failure rate λ). Conversely, if $\Delta N^* = \infty$, i.e., an infinity number of redundant sensors are theoretically deployed, no network failure will be experienced, no matter T; this second extreme case represents *the highest degree of network robustness to node failures*. In-between cases, using a positive but finite number of redundant sensors, are reported in Table 1, which quantifies the degree of robustness of the network.

In particular, Table 1 reports the number of redundant sensors that need to be deployed to compensate for Poisson sensor failures occurring during different observation times under three success probabilities, when $\lambda_1 = 1/(365/12)$, $\lambda_2 = 1/(365/6)$, and $\lambda_3 = 1/(365/4)$ day^{-1}, i.e., in average a sensor experiences one failure every one, two, and three months, respectively. Note that, as the observation time and/or the target success probability increase, a higher numbers of nodes need to be deployed in the body of water. Also, the lower the reliability of individual sensors (which in this simple model is captured by the sensor failure rate λ), the higher the number of redundant nodes required to meet a pre-determined application-specific success probability Γ^*.

5. Deployment in a 3D environment

In this section, we propose three deployment strategies for three-dimensional UW-ASNs to obtain a target *1-coverage* $\eta_1^* = \eta^*$ of the 3D region, i.e., the *3D-random*, the *bottom-random*, and the *bottom-grid* strategies. As previously discussed, it is shown in Ref. [7] that the sensing range r required for 1-coverage is greater than the transmission

Table 1
Redundant sensors ΔN^* to compensate for failures

Observation time T (days)	30	60	90	120	150	180
$\lambda_1 = 1/(365/12)$; $\Gamma_1^* = 0.90$	2	4	5	7	8	9
$\lambda_1 = 1/(365/12)$; $\Gamma_2^* = 0.95$	3	5	6	7	9	10
$\lambda_1 = 1/(365/12)$; $\Gamma_3^* = 0.99$	4	6	8	9	11	12
$\lambda_2 = 1/(365/6)$; $\Gamma_1^* = 0.90$	1	2	3	4	5	5
$\lambda_2 = 1/(365/6)$; $\Gamma_2^* = 0.95$	2	3	4	5	5	6
$\lambda_2 = 1/(365/6)$; $\Gamma_3^* = 0.99$	3	4	5	6	7	8
$\lambda_3 = 1/(365/4)$; $\Gamma_1^* = 0.90$	1	2	2	3	3	4
$\lambda_3 = 1/(365/4)$; $\Gamma_2^* = 0.95$	1	2	3	3	4	5
$\lambda_3 = 1/(365/4)$; $\Gamma_3^* = 0.99$	2	3	4	5	5	6

Please cite this article in press as: D. Pompili et al., Three-dimensional and two-dimensional deployment analysis ..., Ad Hoc Netw. (2008), doi:10.1016/j.adhoc.2008.07.010

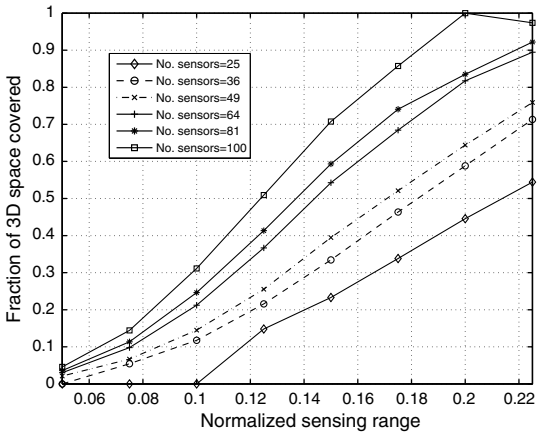

Fig. 15. Three-dimensional scenario: 3D coverage with a 3D-random deployment.

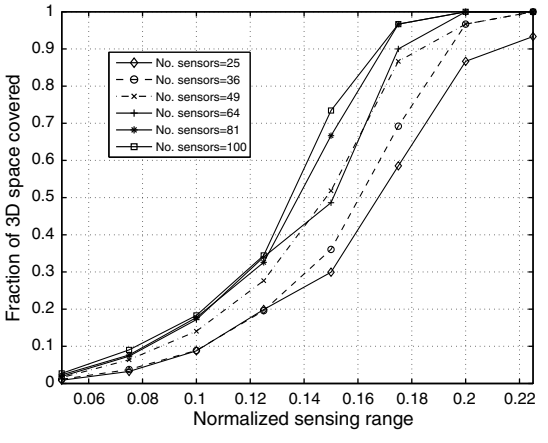

Fig. 16. Three-dimensional scenario: Optimized 3D coverage with a 2D bottom-random deployment.

range t that guarantees network connectivity. Since in typical applications $t \geqslant r$, the network is guaranteed to be connected when 1-coverage is guaranteed. Thus, in the following we focus on the sensing coverage. In all these deployment strategies, winch-based sensor devices are anchored to the bottom of the ocean in such a way that they cannot drift with currents. Sensor devices are equipped with a floating buoy that can be inflated by a pump by means of an electronically controlled engine that resides on the sensor. This way, they can adjust their depth and float at different depths in order to observe a given phenomenon, as described in Section 3.2. In all the proposed deployment strategies, described hereafter, sensors are assumed to know their final positions by exploiting localization techniques.

3D-random. This is the simplest deployment strategy, and does not require any form of coordination from the surface station. Sensors are randomly deployed on the bottom of the 3D volume, where they are anchored. Then, each sensor randomly chooses its depth, and, by adjusting the length of the wire that connects it to the anchor, it floats to the selected depth. Finally, each sensor informs the surface station about its final position.

Bottom-random. As in the previous strategy, sensors are randomly deployed on the bottom, where they are anchored. Differently from the 3D-random scheme, the surface station is informed about their position on the bottom.[1] Then, the surface station calculates the depth for each sensor in order to achieve the target 1-coverage ratio η^*. Finally, each sensor is assigned its target depth and floats to the desired position.

Bottom-grid. This deployment strategy needs to be assisted by one or multiple AUVs, which deploy the underwater sensors to predefined target locations to obtain a grid deployment on the bottom of the ocean. Each sensor is also assigned a desired depth by the AUV and accordingly floats to achieve the target coverage ratio η^*.

Algorithm 1 reports the pseudo code of the procedure run on the surface station to find the optimal depths of the sensor nodes, for the bottom-random and bottom-grid strategies. The positions of the sensor nodes are represented by a matrix $\underline{\mathbf{P}} = [\mathbf{P_1}|\mathbf{P_i}|\mathbf{P_{N-1}}]^T$, where $\mathbf{P_i}$ represents the 3D coordinates of the ith sensor. The Nth node (also N for simplicity) represents the sink, which is located on the surface of the ocean. For example, $\mathbf{P_i}(3)$ represents the z coordinate of the ith sensor. We refer to a discrete set of values, equally spaced with step $step_z$ between 0 (surface) and $z_{\max}$ (ocean bottom), for the depth of the sensor nodes. The function $\hat{\boldsymbol{\eta}}(\underline{\mathbf{P}}, \mathscr{A}, r)$ estimates the coverage ratio η given the positions of the sensors $\underline{\mathbf{P}}$, the target volume $\mathscr{A}$, and their sensing range r.

Algorithm 1. 3D Coverage optimization

```
while (h ⩽ max_steps and η < η*) do
  for (i = 1; i < N; i++) do
    for (j = 0; j ⩽ z_max/step_z; j++) do
      z_old = P_i(3)
      P_i(3) = j * step_z
      η_new = η̂(P, A, r)
      if (η_new > η) then
        η = η_new
      else
        P_i(3) = z_old
      end if
    end for
  end for
  h++
end while
```

Algorithm 1 – presented in Section 5: in the following we calculate the minimum number of sensors needed to achieve a desired target 1-coverage ratio η^* for the proposed deployment strategies.

[1] In shallow water (depth less than 100 m), sensors at the sea-bed can directly communicate to the surface station, while in deep water they should use as relay nodes uw-gateways, which are endowed with short-range horizontal transceivers and long-range vertical transceivers, as described in Section 3.

Please cite this article in press as: D. Pompili et al., Three-dimensional and two-dimensional deployment analysis ..., Ad Hoc Netw. (2008), doi:10.1016/j.adhoc.2008.07.010

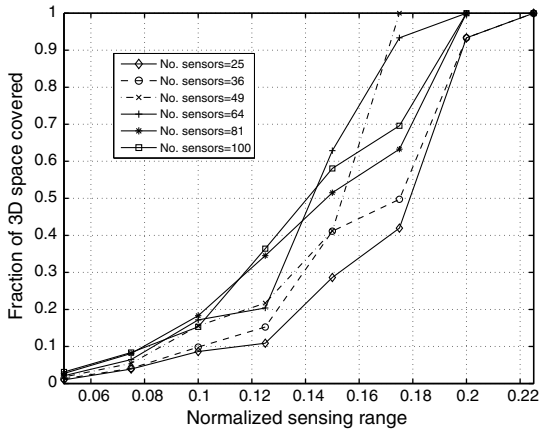

Fig. 17. Three-dimensional scenario: Optimized 3D coverage with a 2D bottom-grid deployment.

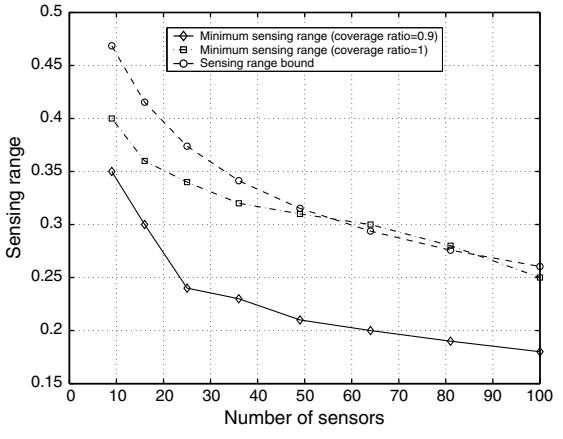

Fig. 18. Three-dimensional scenario: Theoretical and experimental sensing range.

As shown in Figs. 15–17, given a fixed number of sensors we achieve a better coverage ratio with increasing complexity of the deployment strategy. In fact, the coverage ratio obtained with the bottom-grid strategy is greater than the coverage ratio obtained with the bottom-random strategy, which is in turn greater than the coverage ratio of the 3D-random strategy. Moreover, given a target coverage ratio, the minimum number of sensors needed to achieve the desired coverage ratio decreases with the complexity of the deployment strategy. Fig. 18 shows a comparison between the minimum normalized sensing range that guarantees coverage ratios of 1 and 0.9 with the bottom-random strategy and the theoretical bound on the minimum normalized sensing range derived in Ref. [7], where the authors investigate sensing and communication coverage in a 3D environment. According to Theorem 4 in Ref. [7], the 3D volume is guaranteed to be *asymptotically almost surely* 1-covered iff $4/3\pi n/Vr^3 = \ln n + \ln\ln n + \omega(n)$, with $1 << \omega(n) \gg \ln\ln n$, where V is the volume of the region to be covered, n the number of deployed sensors, and r their sensing range. Hence, to draw Fig. 18 we set $\omega(n) = 1 + \ln\ln n/2$. This shows that the bottom-random deployment strategy very closely approximates the theoretically predicted bound, i.e., the minimum sensing range that guarantees 1-coverage with probability 1 is almost the same as that predicted by the model in Ref. [7].

6. Conclusions

In this paper, deployment strategies for two-dimensional and three-dimensional architectures for underwater sensor networks were proposed, and a deployment analysis was carried out, with the objective of determining the minimum number of sensors to achieve application-dependent target sensing and communication coverage; providing guidelines on how to choose the deployment surface area, given a target region; studying the robustness of the sensor network to node failures, while providing an estimate of the number of required redundant sensors.

Acknowledgement

This work was supported by the Office of Naval Research under contract N00014-02-1-0564.

References

[1] I.F. Akyildiz, D. Pompili, T. Melodia, Underwater acoustic sensor networks: research challenges, Ad Hoc Networks (Elsevier) 3 (3) (2005) 257–279.
[2] I.F. Akyildiz, D. Pompili, T. Melodia, State of the art in protocol research for underwater acoustic sensor networks, ACM Mobile Computing and Communication Review 11 (4) (2007).
[3] C. Hsin, M. Liu, Network coverage using low duty cycled sensors: random and coordinated sleep algorithms, in: Proceedings of the IEEE/ACM Conference on Information Processing in Sensor Networks (IPSN), Berkeley, California, April 2004, pp. 433–442.
[4] D. Pompili, T. Melodia, I.F. Akyildiz, Deployment analysis in underwater acoustic wireless sensor networks, in: Proceedings of the ACM International Workshop on UnderWater Networks (WUWNet), Los Angeles, CA, September 2006.
[5] D. Pompili, T. Melodia, I.F. Akyildiz, Routing algorithms for delay-insensitive and delay-sensitive applications in underwater sensor networks, in: Proceedings of the ACM Conference on Mobile Computing and Networking (MobiCom), Los Angeles, LA, September 2006.
[6] J. Proakis, E. Sozer, J. Rice, M. Stojanovic, Shallow water acoustic networks, IEEE Communications Magazine (2001) 114–119.
[7] V. Ravelomanana, Extremal properties of three-dimensional sensor networks with applications, IEEE Transactions on Mobile Computing 3 (3) (2004) 246–257.
[8] R.A. Serway, J.W. Jewett, Physics for Scientists and Engineers, Brooks/Cole, 2004.
[9] S. Shakkottai, R. Srikant, N. Shroff, Unreliable sensor grids: coverage, connectivity, and diameter, in: Proceedings of the IEEE Conference on Computer Communications (INFOCOM), vol. 2, San Francisco, CA, April 2003, pp.1073–1083.
[10] E. Sozer, M. Stojanovic, J. Proakis, Underwater acoustic networks, IEEE Journal of Oceanic Engineering 25 (1) (2000) 72–83.
[11] M. Stojanovic, Acoustic (underwater) communications, in: J.G. Proakis (Ed.), Encyclopedia of Telecommunications, John Wiley and Sons, 2003.
[12] M. Stojanovic, On the relationship between capacity and distance in an underwater acoustic communication channel, in: Proceedings of the ACM International Workshop on UnderWater Networks (WUWNet), Los Angeles, CA, September 2006.
[13] Y. Zou, K. Chakrabarty, Sensor deployment and target localization based on virtual forces, in: Proceedings of the IEEE Conference on Computer Communications (INFOCOM), vol. 2, San Francisco, CA, April 2003, pp. 1293–1303.

Dario Pompili received his Ph.D. in Electrical and Computer Engineering from the Georgia Institute of Technology in June 2007 after working at the Broadband and Wireless Networking Laboratory (BWN-Lab) under the direction of Prof. Akyildiz. In 2005, he was awarded Georgia Institute of Technology BWN-Lab Researcher of the Year for "outstanding contributions and professional achievements". He had previously received his "Laurea" (integrated B.S. and M.S.) and Doctorate degrees in Telecommunications Engineering and System Engineering from the University of Rome "La Sapienza," Italy, in 2001 and 2004, respectively, after working with the DIS Department, advised by Prof. Delli Priscoli. In September 2007, he joined the Electrical and Computer Engineering Department at Rutgers, The State University of New Jersey, as an Assistant Professor. His research interests include ad hoc and sensor networks, underwater acoustic communications, wireless sensor and actor networks, and network optimization and control.

Tommaso Melodia received his Ph.D. in Electrical and Computer Engineering from the Georgia Institute of Technology in June 2007 after working at the Broadband and Wireless Networking Laboratory (BWN-Lab) under the direction of Prof. Akyildiz. He then joined the Electrical Engineering Department at the University at Buffalo, the State University of New York. He had previously received his "Laurea" (equivalent to M.S.) and Doctorate degrees in Telecommunications Engineering from the University of Rome La Sapienza," Rome, Italy, in 2001 and 2005, respectively, after working with the Networking Group of the INFOCOM Department, advised by Prof. Cuomo. His research interests include modeling and optimization of ad hoc and sensor networks, wireless sensor and actor networks, wireless multimedia sensor networks, and underwater acoustic sensor networks.

Ian F. Akyildiz is the Ken Byers Distinguished Chair Professor with the School of Electrical and Computer Engineering, Georgia Institute of Technology and Director of Broadband and Wireless Networking Laboratory. He is the Editor-in-Chief of Computer Networks (Elsevier) and Ad Hoc Networks (Elsevier) Journal. Dr. Akyildiz is an IEEE FELLOW (1995) and an ACM FELLOW (1996). He served as a National Lecturer for ACM from 1989 until 1998 and received the ACM Outstanding Distinguished Lecturer Award for 1994. He received the 1997 IEEE Leonard G. Abraham Prize award (IEEE Communications Society) for his paper entitled "Multimedia Group Synchronization Protocols for Integrated Services Architectures" published in the IEEE Journal of Selected Areas in Communications (JSAC) in January 1996. Dr. Akyildiz received the 2002 IEEE Harry M. Goode Memorial award (IEEE Computer Society) with the citation "for significant and pioneering contributions to advanced architectures and protocols for wireless and satellite networking". Dr. Akyildiz received the 2003 IEEE Best Tutorial Award (IEEE Communication Society) for his paper entitled "A Survey on Sensor Networks", published in IEEE Communication Magazine, in August 2002. He received the 2003 ACM SIGMOBILE award for his significant contributions to mobile computing and wireless networking. His current research interests are in next generation wireless networks, sensor networks, and wireless mesh networks.

Please cite this article in press as: D. Pompili et al., Three-dimensional and two-dimensional deployment analysis ..., Ad Hoc Netw. (2008), doi:10.1016/j.adhoc.2008.07.010